Improved photoelectrocatalytic activities of BiOCl with high stability for water oxidation and MO degradation by coupling RGO and modifying phosphate groups to prolong carrier lifetime

Zhijun Li, Yang Qu, Kang Hu, Muhammad Humayun, Shuangying Chen, Liqiang Jing*

Key Laboratory of Functional Inorganic Materials Chemistry (Heilongjiang University), Ministry of Education, School of Chemistry and Materials Science, International Joint Research Center for Catalytic Technology, Harbin 150080, PR China

ABSTRACT

For an efficient photoelectrocatalysis on bismuth oxychloride (BiOCl), it is highly desired to enhance the photogenerated charge separation and the photochemical stability. Herein, photoelectrocatalytic activities of BiOCl photoanodes for water oxidation to evolve O_2 and for methyl orange (MO) degradation have been greatly improved through firstly coupling with reduced graphene oxide (RGO) and then modifying with phosphoric acid. It is shown that the optimal amount of phosphate modified RGO/BiOCl nanocomposite photoanode exhibits 3.8-time and 8.4-time activity enhancement respectively for water oxidation and MO degradation, compared to the bare BiOCl. It is confirmed that the improved activities are attributed to enhanced charge separation and prolonged carrier lifetime of BiOCl after chemically coupling with RGO to collect electrons and modifying with phosphate groups to trap positive holes via the formed negative field on the surfaces, mainly based on electrochemical impedance spectra, time-resolved surface photovoltage responses, and produced hydroxyl radical amounts. Moreover, it is concluded that the phosphate groups are modified on BiOCl by replacing photochemically-unstable chloride ions, consequently leading to the enhanced stability. Expectedly, this positive strategy is also applicable to the visible-response BiOBr as an efficient photoanode. This work opens up a feasible route to efficiently improve the PEC performance of BiOX-based nanomaterials with high stability.

© 2016 Elsevier B.V. All rights reserved.

1. Introduction

Photoelectrocatalytic (PEC) water splitting and organic pollutant degradation on semiconductor photoelectrodes have been demonstrated to be effective techniques for energy production as the alternative to fossil fuels and for environmental remediation [1–4]. In this regard, numerous semiconductor photocatalysts have been explored as photoanode materials, such as TiO_2, $BiVO_4$, Fe_2O_3 and so on [5–7]. However, the development of new and effective photocatalysts is still under investigation, since the current PEC efficiency is low for practical application. In recent years, BiOCl has attracted considerable attention in the field of photocatalysis for organic pollutant degradation and water oxidation owing to its suitable valence-band (VB) position [8], special layered structure [Cl-O-Bi-O-Cl] [9], and structure-dependent photocatalytic performance [10,11]. However, the weak charge separation and poor

stability of BiOCl still limit its wide use for PEC water oxidation and pollutant degradation greatly [12,13]. Therefore, it is highly desired to enhance the photogenerated charge separation and the photochemical stability of BiOCl for efficient photocatalysis and/or photoelectrocatalysis.

In order to enhance the charge separation, some efforts have been made, including facet and band engineering [14,15], doping [16], modification and coupling [17,18]. Among those strategies, heterojunction with other materials, such as Ag, Au, carbon quantum dots, and graphene, is often taken as a feasible route for efficient photocatalysis [19–22]. Considering the unique 2D planar structure and rich surface groups as well as electron accepting and transferring ability of the RGO, it is much feasible for efficient photocatalysis to construct heterojunctions between BiOCl and RGO [23]. In particular, the strong C-Bi chemical bonds might be formed, which would further improve the photocatalytic performance of BiOCl under UV light irradiation [24]. Therefore, it is expected that the activity of BiOCl photoanodes for PEC oxidation would be improved by chemically coupling with RGO.

O_2 production is a four-electron process and considered as the rate-determining step for water splitting [25]. Hence, it is of great significance to improve the activity of BiOCl for water oxidation to evolve O_2. As a kind of electric species, the positively charged holes could easily be transferred to the surface if there is a surface negative electrostatic field. In addition, the stability of photoelectrode is much important for practical applications. Recently Carmalt et al. demonstrated that BiOCl photoelectrode display poor stability due to photocorrosion [13]. The relative research by Yukiko Fujishima et al. demonstrated that BiOCl is unstable in aqueous solution under UV-light irradiation, and easily produce Cl-vacancies by the loss of Cl [26]. This phenomenon may be related to the poor stability of BiOCl photoanode. Hence, it is necessary to clarify the effect of Cl or Cl-vacancies in BiOCl. Based on the above consideration, it is much meaningful to substitute the unstable surface Cl with other more stable and effective anions to induce the holes from bulk to surface so as to promote the charge separation, simultaneously improving the stability of BiOCl photoanode.

In our previous works [27,28], it is clearly demonstrated that the phosphate modification could promote the charge separation of TiO_2 or $BiVO_4$ in water so as to improve the PEC performance for water oxidation. The enhancement is attributed to the formed negative field on the semiconductor surfaces by the fixed phosphate groups. Thus, it is a promising approach to improve the stability as well as charge separation of BiOCl photoanode by substituting the unstable Cl with stable phosphate groups.

Herein, we report an interesting and effective method for improving charge separation and stability of BiOCl photoanode by coupling RGO and then modifying with phosphate groups. It is obvious that the PEC performance for water oxidation and organic dye degradation is significantly improved, which is attributed to the acceleration of transferring photogenerated electrons by coupling RGO and the replacement of unstable Cl by phosphate groups. It is concluded that the phosphate groups not only induces the migration of photogenerated holes via ionized negative field but also improve the stability of BiOCl photoanode. Thus, this work provides a feasible route to improve the photocatalytic/photoelectrochemical performance of BiOX-based nanomaterials.

2. Experimental

2.1. Reagents

All the reagents were of analytical grade and used as received without further purification. Deionized water was used throughout.

2.2. Photocatalyst synthesis

2.2.1. Preparation of BiOCl

BiOCl nanoplates (BOC) were prepared according to the previous report [10]. In a typical experiment, equimolar amount (1 mmol) of $Bi(NO_3)_3 \cdot 5H_2O$ and KCl were dissolved in 30 mL of distilled water under continuous stirring at room temperature (~25 °C). The solution was stirred for 30 min and then transferred to a 50 mL of Teflon-lined stainless autoclave. The autoclave was hydrothermally treated at 160 °C for 6 h under autogenous pressure. After cooling to room temperature, the resulting precipitate was collected and washed several times with ethanol and deionized water. The product was finally dried at 60 °C in air to obtain the powder sample.

2.2.2. Preparation of RGO/BiOCl nanocomposites

Graphene oxide (GO) as a precursor was introduced during the synthesis of RGO/BiOCl hybrids, which was prepared by a modified Hummers method [29]. In a typical experiment for

obtaining 5G/BOC (mass ratio of GO:BiOCl is 5:100) 0.5 g of the as-prepared BiOCl nanoplates were dispersed in 10 mL ethanol and continuously stirred for 30 min. After that, 2.5 mL of GO solution (10 mg/mL) was added into the above reaction mixture and deionized water was added to the mixture to raise its volume up to 20 mL. The reaction mixture was covered with plastic wrap and ultrasonically treated for 30 min, followed by magnetic stirring for 2 h. Then the mixture was transferred to a 50 mL Teflon-lined stainless-steel autoclave and hydrothermally treated at 120 °C for 3 h. After cooling to room temperature naturally, the obtained products were collected and washed thoroughly with deionized water followed by absolute ethanol. Finally, the samples were dried in air at 60 °C for 4 h. Other samples xG/BOC (x = 10, 15, 20) were prepared by the same procedure just with addition of different mass concentration of GO solution. For comparison, pure BOC was also prepared by the same method just without the addition of GO.

2.2.3. Phosphate modified 15G/BOC photoanodes

All of the xG/BOC photoanode films were prepared by a doctor blade method. The pastes were prepared according to the following procedure: In a typical synthesis, 0.5 g powder sample was dispersed in 2 mL isopropyl alcohol and ultrasonically treated for 30 min followed by magnetic stirring for 30 min. After that, 0.25 g of Macrogol-6000 was added to the above reaction system and ultrasonically treated for another 30 min followed by magnetic stirring for 30 min. Subsequently, 0.1 mL of acetyl acetone was added to the reaction mixture and continuously stirred for 48 h in order to obtain the paste. Conductive fluorine doped tin oxide (FTO)-coated glasses were washed in acetone for 30 min under ultrasonic treatment, followed by washing with deionized water. These glasses were used as substrates for the films preparation. Prior to use, the FTO glasses were sintered at 450 °C for 30 min. The sample films were fabricated by a doctor blade method using scotch tape as the spacer. The films were dried in air for 30 min, and then sintered at 400 °C for 30 min. After cooling to room temperature naturally, the sample films were cut into 2.0 cm × 3.0 cm pieces with film surface area of 2.0 cm × 2.0 cm.

The phosphate modified 15G/BOC photoanodes were prepared by impregnation method. In a typical experiment, the 15G/BOC films were suspended into a desired concentration of phosphoric acid solution (10 mL) for 30 min. After that, the film were rinsed with deionized water, dried naturally in air for 6 h and finally sintered at 350 °C for 30 min. The as-prepared phosphate modified nanocomposites were represented by xP-G/BOC, where x is the molar concentration of phosphoric acid solution.

2.3. Catalyst characterization

The different samples were characterized by X-ray diffraction (Rigaku D/MAX-RA diffractometer, Japan). Electron micrographs were taken by a JEOL JEM-2010 transmission electron microscope. Scanning electron microscopy (SEM) images were taken using a Hitachi S-4800 instrument operating at 15 KV. The UV–vis absorption spectra were recorded with a Model Shimadzu UV-2550 spectrophotometer. Transmission electron microscopy (TEM) micrographs were taken with a JEOL JEM-2010 (Japan) operated at an accelerating voltage of 200 kV.

The surface composition and elemental chemical states of the films were measured by X-ray photoelectron spectroscopy (XPS) using a Kratos-Axis Ultra DLD apparatus equipped with an Al (mono) X-ray source. The binding energies of the sample films were calibrated with respect to the signal for adventitious carbon (binding energy 284.6 eV). Raman spectra were performed with a Jobin Yvon HR 800 micro-Raman spectrometer at 457.9 nm. The laser beam was focused with a 50 × objective lens to a ca. 1 μm spot on the surface of the sample. The photoluminescence spectra of the

solid samples were measured with a PE LS 55 spectrofluorophotometer at excitation wavelength of 350 nm.

The steady-state surface photovoltage spectra (SS-SPS) were measured with a home-built apparatus as discussed elsewhere [30]. During the measurement, the sample chamber was connected to an ITO glass as the top electrode and to a steel substrate as the bottom electrode, and about 10 μm thick mica spacer was placed between the ITO glass and the film to decrease the space charge region at the ITO-sample interface. The time-resolved surface photovoltage (TR-SPV) signals of the photoanode films were measured in Na_2SO_4 solution (0.5 M) and bubbled with N_2 for 30 min before test, with a home-built device [28], and then the films were excited under laser irradiation of wavelength 355 nm with 10 ns pulse width from a second harmonic Nd:YAG laser (Lab-130-10H, Newport, Co.). The intensity of the laser was modulated with an optical neutral filter and measured by a high energy pyroelectric sensor (PE50BF-DIF-C, Ophir Photonics Group). The signals were recorded with a 1 GHz digital phosphor oscilloscope (DPO 4104B, Tektronix) connected to an amplifier with the aid of a computer.

2.4. PEC measurements

PEC measurements of the sample films were performed with three-electrode configuration using an Ag/AgCl reference electrode and a Pt foil counter electrode, and 0.5 M Na_2SO_4 solution (pH = 7) was used as the electrolyte under room temperature. The photoelectrodes were illuminated with a 150 W Xenon lamp. The applied potential was controlled using a commercial computer controlled potentiostat (AUTOLAB PG STAT 101). Oxygen-free nitrogen gas was bubbled through the electrolyte before and during the experiments for films test.

The PEC oxygen evolution experiments were performed in a sealed quartz cell. In a typical experiment, the film electrodes used as working electrodes were dipped in 80 mL of 0.5 M Na_2SO_4 electrolyte and pure oxygen-free nitrogen gas was bubbled through the electrolyte solution for 90 min prior to the measurement. The sample films were irradiated from the FTO glass side, whose working area was approximately $2 \times 2\,cm^2$ at applied voltage of +0.6 V vs Ag/AgCl electrode. The amount of oxygen was measured with Marine optical oxygen sensor by dipping the needle probe into the electrolyte solution near working electrode. During measurement, the film was irradiated for 800 s with a 150 W xenon light source.

During the measurements of PEC degradation of methyl orange (MO), the as-prepared films were used as working electrodes, a Pt plate as counter electrode, and the applied bias was +0.6 V. The films were dipped in a sealed quartz cell containing 30 mL of 0.5 M $Na_2SO_4/20\,mg\,L^{-1}$ MO aqueous solution as electrolyte. The EC and PC experiments for pollutant degradation were performed in the same way by varying the reaction conditions. The pure air was bubbled through the electrolyte solution and kept in dark for 15 min to reach the adsorption saturation. After that, the film was irradiated with a 150 W Xe-light (radiation source) for 15 min, and a certain amount of the reacted MO solution was transferred into a pyrex glass cell for the UV–vis absorption at 456 nm, through a Shimadzu UV-2550 spectrophotometer, and repeated the process for the study of MO degradation kinetics by changing the reaction time (30 min, 45 min, 60 min).

For PEC hydroxyl radical measurement, the as-prepared films were used as working electrodes. The films were dipped in a sealed quartz cell containing 30 mL of 0.5 M $Na_2SO_4/0.001$ M coumarin aqueous solution as electrolyte. The pure air gas was bubbled through the electrolyte solution and irradiated with 150 W Xe-light (radiation source) for 30 min before the measurement. After irradiation for 30 min, a certain amount of the coumarin reacted solution was transferred into a pyrex glass cell for the fluorescence measurement of 7-hydroxycoumarin at about 460 nm with excitation

wavelength 332 nm, through a spectrofluorometer (PerkinElmer LS55).

Electrochemical impedance spectra (EIS) were measured using a three-electrode configuration with the Princeton Applied Research Versa STAT 3 and carried out over the frequency range from 10^2 to 10^5 Hz with amplitude of 10 mV (RMS) at the bias of +0.4 V in a 0.5 M Na_2SO_4 solution.

3. Results

3.1. Structural characterization and surface composition

From SI-Fig. 1A, it is found that the X-ray diffraction patterns of bare BOC and xG/BOC nanocomposites are in good agreement with tetragonal PbFCl-type BiOCl (JCPDS File no. 06-0249) [10]. Moreover, the results show that the amount of RGO does not influence the crystal phase of BiOCl, and the intensity of the samples decreased with the increase in amount of RGO, which may result from the reduced proportion of BiOCl [31]. SI-Fig. 1B shows the Raman spectra of BOC and xG/BOC nanocomposites. It is shown that BOC do not exhibit Raman bands in the range of 1000–2000 cm^{-1}. However, xG/BOC films exhibit two strong Raman peaks at 1355 and 1604 cm^{-1}, which are respectively attributed to the D and G bands of coupled RGO. It is obvious that these bands are slightly enhanced with the increase in the amount of coupled RGO [32].

The morphology of BOC sample was investigated by SEM. From SI-Fig. 1C, it is clear that BOC exhibit nanoplate-like morphology with thickness in the range of 80–300 nm. The TEM image of 15G/BOC (SI-Fig. 1D), further reveals that RGO is uniformly coupled with BOC nanoplates. Moreover, the single crystalline tetragonal structure of BOC is confirmed from the SAED patterns as shown in SI-Fig. 1D inset [10]. The UV–vis diffuse reflectance spectra (SI-Fig. 2) of BOC and xG/BOC samples reveal that the introduction of RGO does not change the bandgap of BOC and the optical absorption across the bandgap edge is 3.45 eV, based on the widely accepted energy bandgap equation Eg = 1240/λ [33]. Moreover, the intensity of diffuse reflectance related to xG/BOC nanocomposites decreased with the increase in RGO content. This is because RGO shows strong absorption in visible light range.

The XPS analysis is employed to study the elemental states and chemical composition of 15G/BOC and xP-G/BOC sample films. From Fig. 1A, it is clear that 15G/BOC do not show XPS peak at 133.8 eV, while xP-G/BOC samples exhibit strong signals at this position, which are attributed to P2p orbital [27]. These peaks are obviously enhanced with increase in phosphate amount. The Bi4f XPS spectra (Fig. 1B) clearly indicate that BOC exhibit two bands located at 159.2 and 164.5 eV, which are attributed to the Bi (4f7/2) and Bi (4f5/2) spin orbital splitting photoelectrons [24]. For 15G/BOC film, the binding energies of Bi (4f 7/2) and Bi (4f 5/2) are located at 159.8 and 165.1 eV, respectively. These peaks are slightly shifted towards higher binding energy as compared to the pure BOC, which proves the presence of strong interaction between RGO and BOC [32]. Similarly, the two peaks of xP-G/BOC are slightly shifted toward higher binding energy compared to the 15G/BOC, which means the phosphate groups are successfully modified on the surfaces of BOC. This is further confirmed by the XPS analysis of percentage amount of Cl and P element, shown in Table 1 (SI). It is noticed that the amount of Cl is obviously decreased with the increase in P content, implying that P substituted the Cl to a certain degree.

Fig. 2A shows the XRD patterns of BOC, 15G/BOC and 0.005P-15G/BOC films. It is clear that the phosphate modification does not change the crystal phase and crystallinity of 15G/BOC nanocomposite film. The SEM micrograph of BOC film is shown in Fig. 2B. It is obvious that BOC nanoplates overlap on the FTO substrate,
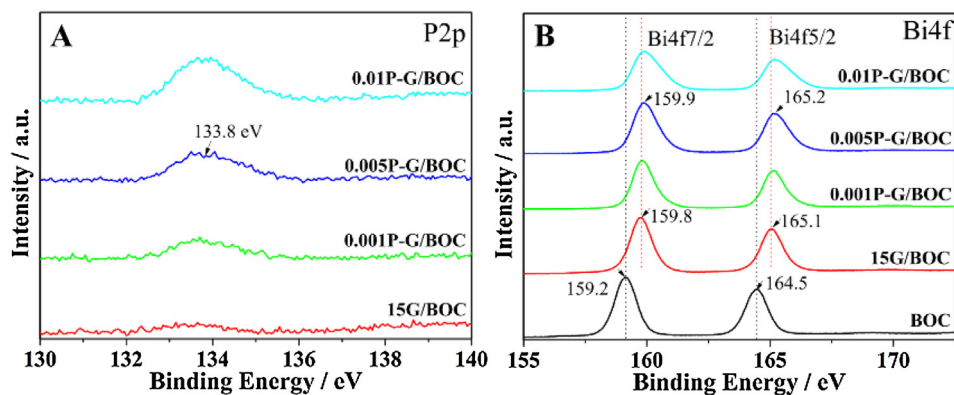
Fig. 1. XPS spectra of P2p (A) and Bi4f (B) of the as-prepared xP-G/BOC films.
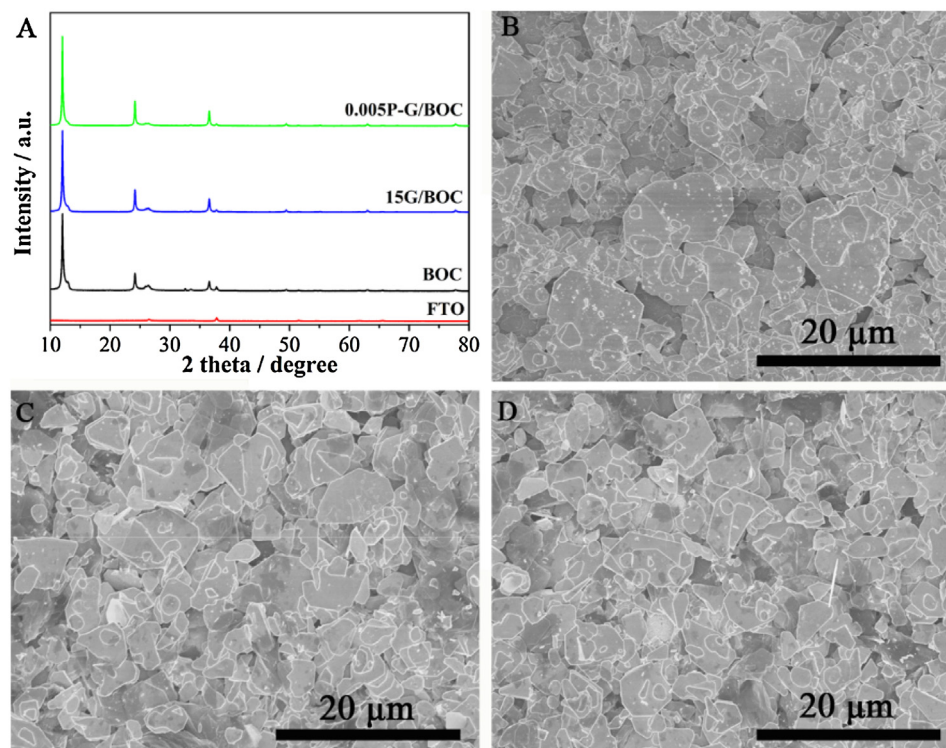

Fig. 2. XRD patterns (A) and SEM images of BOC (B), 15G/BOC (C) and 0.005P-G/BOC (D) films.

which means much effective contact. As expected, the morphology of 15G/BOC film (Fig. 2C) is slightly different from BOC one. In addition, it is noticed that some dark component (RGO) appeared on the surfaces of BOC nanoplates, and the phosphate modification does not affect the morphology of 15G/BOC film.

3.2. PEC activities for water oxidation and MO degradation

The photocurrent densities of BOC and xG/BOC samples are shown in Fig. 3A. It is clear that BOC film shows a low photocurrent density response under UV–vis light, while the photocurrent density response of xG/BOC films is remarkably enhanced, especially for 15G/BOC film. This suggests that coupling a proper amount of RGO is favorable for charge transfer and separation in BOC and the over excess amount further leads to the poor activity because of light shading by RGO [24]. The photocurrent density measurements were carried out to study the effect of phosphate modification on the activity of 15G/BOC films, as shown in Fig. 3B. It can be seen that

the photocurrent density response of the optimized 15G/BOC film is obviously enhanced after phosphate modification and the significant enhancement is observed for 0.005P-G/BOC film. To prove this, transient photocurrent density responses of BOC, 15G/BOC and 0.005P-15G/BOC films were measured as shown in Fig. 3B inset. It is demonstrated that BOC film exhibits very low transient current response, however, it is obviously enhanced for 15G/BOC film and further increased is observed for 0.005P-15G/BOC film. Hence, it is suggested that the charge transfer and separation in BOC can be obviously improved after coupling RGO and then modifying with phosphoric acid.

This is further supported by the PEC O_2 evolution experiments and stability tests. As shown in Fig. 3C, BOC film exhibits a very small amount of O_2 evolved and also its stability is poor. In comparison, the amount of O_2 evolved by 15G/BOC film is very large by about 2.4-fold enhanced as compared to BOC film, but its stability is still not good enough. Interestingly, it is observed that 0.005P-15G/BOC film exhibits significant amount of O_2 (about 3.8-fold enhanced as
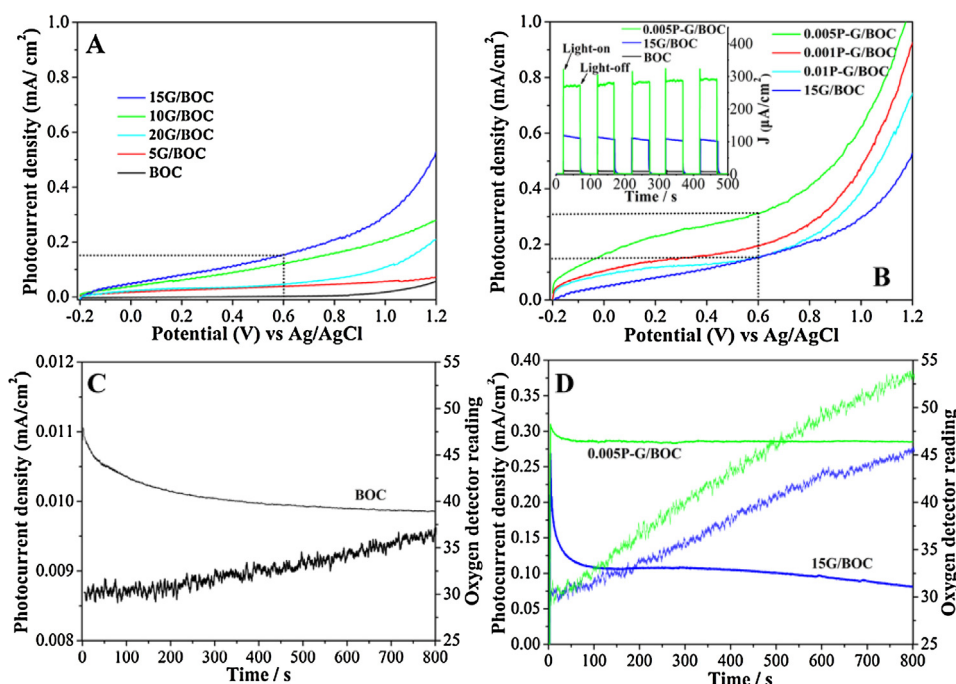
Fig. 3. Photocurrent density response (I–V curves) of xG/BOC films (A) and xP-G/BOC films (B) with inset transient photocurrent response of BOC, 15G/BOC and 0.005P-G/BOC films, PEC O$_2$ evolution test (rough line) of BOC film with inset stability test (smooth line) (C), PEC O$_2$ evolution test (rough line) of 15G/BOC and 0.005P-G/BOC films with inset stability test (smooth line) (D).
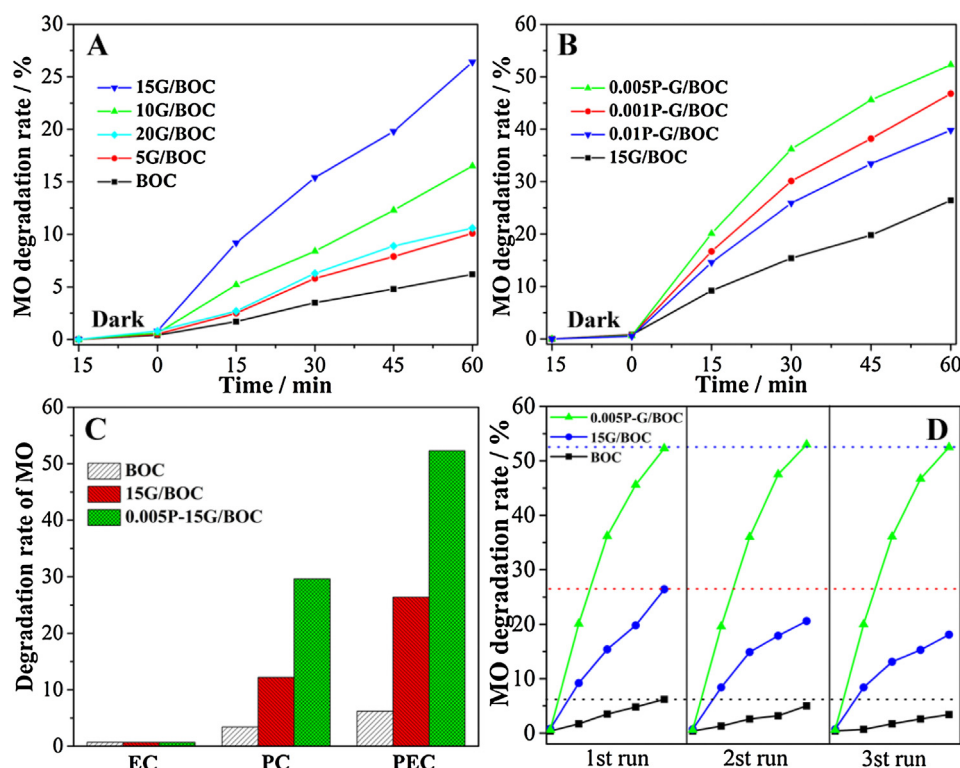

Fig. 4. PEC degradation kinetic curves of MO over BOC and xG/BOC films (A) and xP-G/BOC films (B), the EC, PC and PEC degradation kinetic curves of MO over BOC, 15G/BOC and 0.005P-G/BOC films (C), stability test for the PEC degradation of MO over the BOC, 15G/BOC and 0.005P-G/BOC films (D).

compared to BOC film) as shown in Fig. 3D. Notably, its stability is remarkably high as compared to that of 15G/BOC film.

In order to further evaluate the PEC activity of BOC, xG/BOC and xP-G/BOC films for pollutant degradation, MO is chosen as model pollutant due to its high toxic and chemically stable nature [34].

The degradation kinetic curves of BOC and xG/BOC films are shown in Fig. 4A. It can be seen clearly that the degradation kinetic rate of BOC film is greatly improved after coupling RGO. Interestingly, the MO degradation rate of 15G/BOC film is found to be higher than that of bare BOC film by about 4.3 times. Fig. 4B shows the
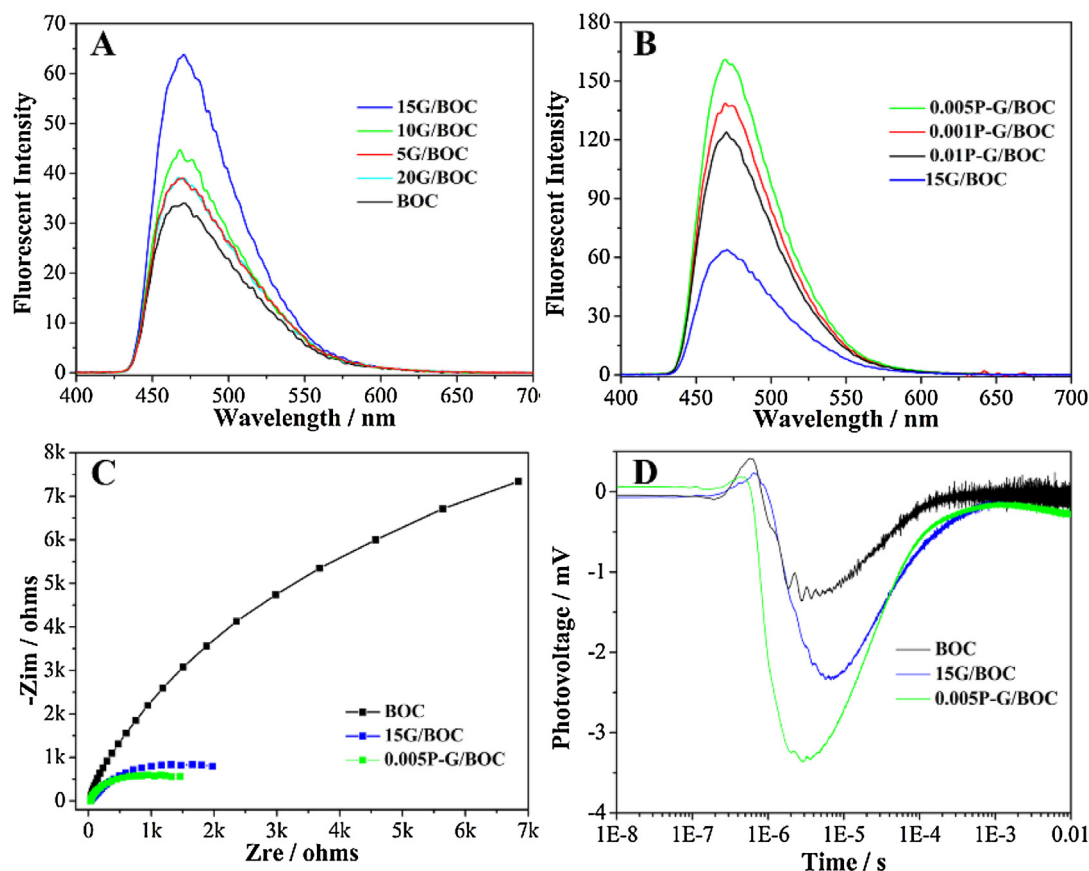
Fig. 5. Fluorescence emission intensity peaks related to $^{\bullet}OH$ amount produced of xG/BOC films (A) and xP-G/BOC films (B), electrochemical impedance spectra (EIS) (C) and TR-SPV responses (D) of BOC, 15G/BOC and 0.005P-G/BOC films.

PEC activity of 15G/BOC and xP-G/BOC films for MO degradation. It can be seen that the degradation kinetic curves of 15G/BOC film is remarkably enhanced after phosphate modification and the highest activity is observed for 0.005P-G/BOC film, which is about 8.4-time enhancement compared to the bare BOC film.

To further prove the enhanced degradation activity of different films, we have measured electrochemical (EC) and photochemical (PC) activities of BOC, 15G/BOC and 0.005P-G/BOC films. As shown in Fig. 4C, all the films exhibit very low EC activity for MO degradation. Moreover, the PC activity is much higher as compared to EC ones, and the PEC activity is significant. Hence, it is suggested that coupling a proper amount of RGO and then modifying with phosphoric acid can greatly enhance PEC activity for MO degradation, and the most important point is that the poor stability of BOC and 15G/BOC can be improved, as shown in Fig. 4D.
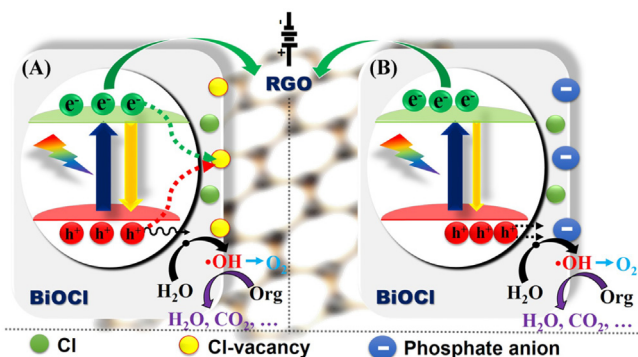
4. Discussion

It is widely accepted that the hydroxyl radical ($^{\bullet}OH$) is usually taken as the intermediate products for O_2 evolution and pollutants degradation [35]. In general, the coumarin easily reacts with $^{\bullet}OH$ to produce luminescent 7-hydroxycoumarin. Hence, coumarin fluorescent method is used to measure the amount of $^{\bullet}OH$ produced by the sample films. As shown in Fig. 5A, it is obvious that the fluorescence emission intensity related to $^{\bullet}OH$ of BOC film is remarkably enhanced after coupling RGO and the highest intensity is observed for 15G/BOC sample. Moreover, Fig. 5B reveals that the phosphate modification further enhances the produced $^{\bullet}OH$ radical amount and the significant amount is observed for 0.005P-15G/BOC film. However, the over excess amount of phosphoric acid

is unfavorable for further increase in the formed $^{\bullet}OH$ radicals, as for 0.1P-15G/BOC sample. These results are well consistent with the produced O_2 amount, and the MO degradation rate, which means improved photogenerated charge separation.

To further gain insight into the effects of coupling RGO and phosphate modification on the photogenerated charge carrier separation behavior, the electrochemical impedance spectra Nyquist plots of BOC, 15G/BOC and 0.005P-15G/BOC films were measured as shown in Fig. 5C. In general, the smaller radius always represents low charge transfer resistance. It is demonstrated that under UV–vis irradiation, the arc radius of 15G/BOC film is obviously decreased as compared BOC film, suggesting that the conductivity is greatly improved after introducing RGO. Moreover, the arc radius of 0.005P-15G/BOC film is further decreased as compared to 15G/BOC. Hence, it is suggested that the phosphate modification play a vital role in the charge separation of 15G/BOC film because of the surface-carried negative charge resulting from the dissociation of modified phosphate groups [28]. In order to confirm the prolonged life-time and separation of photogenerated charges directly, the TR-SPV responses of BOC, 15G/BOC and 0.005P-15G/BOC films were measured in the solution environment as shown in Fig. 5D. All the films exhibit negative TR-SPV responses in Na_2SO_4 electrolyte solution. It is obvious that BOC film shows a low TR-SPV response, however, 15G/BOC film shows enhanced TR-SPV signal and the significant response is observed for 0.005P-15G/BOC film. Hence, it is suggested that the charge separation and carrier lifetime of BOC can be significantly improved after coupling RGO and then modifying with phosphoric acid.

More interesting, the poor stability of BOC is obviously improved after coupling RGO and then modifying with phosphoric acid.

Scheme 1. Proposed mechanism for the photogenerated charge transfer and separation in RGO/BOC photoanodes before (A) and after phosphate modification (B).

Hence, it is necessary to investigate the effect of Cl. Thus, the SS-SPS and TR-SPV measurements are employed. The SS-SPS signals of BOC in different atmosphere are shown in SI-Fig. 3A. It is clear that BOC shows an obvious SPS signal in N_2 atmosphere, however, the SPS response intensity is remarkably decreased in air and O_2 atmosphere. Hence, it is suggested that some special species of BOC would act as donators to trap the photogenerated holes and the corresponding electrons will preferentially diffuse to the testing electrode surfaces. This is further supported by the TR-SPV signal of BOC (inset of SI-Fig. 3A), under laser pulse irradiation of wavelength 355 nm. It is shown that the sample exhibits negative TR-SPV response in air, which is attributed to the holes trapped by the special specie. This special specie is suspected to be Cl according to our previous works [36].

In order to confirm this, Cl-vacancies are introduced in BOC by UV–vis light irradiation in water and taken as a reference sample (denoted as BOC-vac). The Cl 2p XPS of BOC and BOC-vac samples are shown in SI-Fig. 3B. It is obvious that the XPS peaks of Cl 2p at binding energies 197.9 and 199.5 eV, are remarkably decreased in the BOC-vac sample, confirming the generation of Cl-vacancies. The photoluminescence spectra is a highly sensitive and non-destructive technique and widely used to investigate the information about surface defects and vacancies. Generally speaking, the high PL signal indicates the high charge recombination rate. From SI-Fig. 3C, it is clear that BOC exhibits a low PL signal, however, the PL signal is greatly enhanced after generation of Cl-vacancies. These results suggest that chloride vacancies are harmful to photogenerated charge separation, and play as a recombination center, as shown in Scheme 1(A). Fortunately, the unstable chloride in BOC can be replaced with phosphate groups after modification, which not only reduce the recombination centers, but also favorable to induce the photogenerated holes to the surface of BOC so as to improve the separation of photogenerated charges, as shown in Scheme (B). Thus, both the charge separation and stability of 15G/BOC could be improved. Besides that, this strategy is versatile for BiOX materials that could be extended to BiOBr photoanode to improve the PEC activities as well, as shown in SI-Fig. 4. The RGO-coupled BiOBr have been successfully prepared and then modified with phosphoric acid. As expected, the PEC performance of BiOBr photoanode is also obviously improved.

5. Conclusions

In summary, the stability and photoelectrochemical performance of BOC photoanodes are obviously improved after coupling RGO and then modifying with phosphoric acid. It is demonstrated that the highly stable 0.005P-15G/BOC photoanode exhibits enhanced PEC activities for water oxidation and MO degradation, as compared to the bare BOC photoanode. The improved PEC

activities are mainly attributed to the enhanced charge separation and prolonged carrier lifetime of BiOCl after chemically coupling with RGO to accept electrons and modification with phosphate groups to trap positive holes via the formed negative field on the surfaces. The modified phosphate groups could substitute the unstable Cl on the surfaces to favor the holes transfer to the photoanode surfaces, simultaneously improving the stability. This developed strategy is feasible for BiOX materials to improve the PEC activities.

Acknowledgments

Appendix A. Supplementary data

Supplementary data associated with this article can be found, in the online version, at http://dx.doi.org/10.1016/j.apcatb.2016.10.045.

References

[1] M.G. Walter, E.L. Warren, J.R. McKone, S.W. Boettcher, Q. Mi, E.A. Santori, N.S. Lewis, Chem. Rev. 110 (2010) 6446–6473.
[2] J. Su, L. Zhu, G. Chen, Appl. Catal. B: Environ. 186 (2016) 127–135.
[3] Y.-f. Su, G.B. Wang, D.T.F. Kuo, M.l. Chang, Y.-h. Shih, Appl. Catal. B: Environ. 186 (2016) 184–192.
[4] Z.S. Li, J.Y. Feng, S.C. Yan, Z.G. Zou, Nano Today 10 (2015) 468–486.
[5] Z.F. Huang, L. Pan, J.J. Zou, X. Zhang, L. Wang, Nanoscale 6 (2014) 14044–14063.
[6] H.M. Nguyen, C.M. Phan, T. Sen, S.A. Hoang, Desalin. Water Treat. 57 (2016) 14379–14385.
[7] A. Fujishima, K. Honda, Nature 238 (1972) 37–38.
[8] X. Zhang, B. Li, J. Wang, Y. Yuan, Q. Zhang, Z. Gao, L.M. Liu, L. Chen, Phys. Chem. Chem. Phys. 16 (2014) 25854–25861.
[9] J. Li, Y. Yu, L. Zhang, Nanoscale 6 (2014) 8473–8488.
[10] J. Jiang, K. Zhao, X. Xiao, L. Zhang, J. Am. Chem. Soc. 134 (2012) 4473–4476.
[11] Y. Wu, B. Yuan, M. Li, W.H. Zhang, Y. Liu, C. Li, Chem. Sci. 6 (2015) 1873–1878.
[12] J. Li, L. Cai, J. Shang, Y. Yu, L. Zhang, Adv. Mater. 21 (2016) 4059–4064.
[13] D.S. Bhachu, S.J.A. Moniz, S. Sathasivam, D.O. Scanlon, A. Walsh, S.M. Bawaked, M. Mokhtar, A.Y. Obaid, I.P. Parkin, J. Tang, C.J. Carmalt, Chem. Sci. 8 (2016) 4832–4841.
[14] L. Ye, L. Zan, L. Tian, T. Peng, J. Zhang, Chem. Commun. 47 (2011) 6951–6953.
[15] L. Wang, J. Shang, W.C. Hao, S.Q. Jiang, S.H. Huang, T.M. Wang, Z.Q. Sun, Y. Du, S.X. Dou, T.F. Xie, D.J. Wang, J. Wang, Sci. Rep. 4 (2014), srpe 07384.
[16] Z. Jiang, Y. Liu, T. Jing, B. Huang, Z. Wang, X. Zhang, X. Qin, Y. Dai, RSC Adv. 5 (2015) 47261–47264.
[17] L. Zhang, W. Wang, S. Sun, D. Jiang, E. Gao, Appl. Catal. B: Environ. 162 (2015) 470–474.
[18] S. Ning, L. Ding, Z. Lin, Q. Lin, H. Zhang, H. Lin, J. Long, X. Wang, Appl. Catal. B: Environ. 185 (2016) 203–212.
[19] H. Lin, L. Ding, Z. Pei, Y. Zhou, J. Long, W. Deng, X. Wang, Appl. Catal. B: Environ. 160 (2014) 98–105.
[20] J. Di, J. Xia, M. Ji, B. Wang, S. Yin, Q. Zhang, Z. Chen, H. Li, ACS Appl. Mater. Interfaces 7 (2015) 20111–20123.
[21] H. Li, L. Zhang, Nanoscale 6 (2014) 7805–7810.
[22] S. Dong, Y. Pi, Q. Li, L. Hu, Y. Li, X. Han, J. Wang, J. Sun, J. Alloys Compd. 663 (2016) 1–9.
[23] D. Chen, H. Zhang, Y. Liu, J. Li, Energy Environ. Sci. 6 (2013) 1362–1387.
[24] F. Gao, D. Zeng, Q. Huang, S. Tian, C. Xie, Phys. Chem. Chem. Phys. 14 (2012) 10572–10578.
[25] J. Tang, J.R. Durrant, D.R. Klug, J. Am. Chem. Soc. 130 (2008) 13885–13891.
[26] Y. Fujishima, S. Okamoto, M. Yoshiba, T. Itoi, S. Kawamura, Y. Yoshida, Y. Ogura, Y. Izumi, J. Mater. Chem. A 3 (2015) 8389–8404.
[27] L. Jing, J. Zhou, J.R. Durrant, J. Tang, D. Liu, H. Fu, Energy Environ. Sci. 5 (2012) 6552–6558.
[28] M. Xie, J. Bian, M. Humayun, Y. Qu, Y. Feng, L. Jing, Chem. Commun. 51 (2015) 2821–2823.
[29] K.S. Novoselov, A.K. Geim, S.V. Morozov, D. Jiang, Y. Zhang, S.V. Dubonos, I.V. Grigorieva, A.A. Firsov, Science 306 (2004) 666–669.
[30] L. Jing, S. Li, S. Song, L. Xue, H. Fu, Sol. Energy Mater. Sol. Cells 92 (2008) 1030–1036.

[31] H. Tang, Y. Ao, P. Wang, C. Wang, Mater. Sci. Semicond. Process. 27 (2014) 909–914.
[32] L. Tian, J. Liu, C. Gong, L. Ye, L. Zan, J. Nanopart. Res. 15 (2013) 1917.
[33] M. Humayun, A. Zada, Z.J. Li, M.Z. Xie, X.L. Zhang, Y. Qu, F. Raziq, L.Q. Jing, Appl. Catal. B: Environ. 180 (2016) 219–226.
[34] L. Sun, L. Xiang, X. Zhao, C.-J. Jia, J. Yang, Z. Jin, X. Cheng, W. Fan, ACS Catal. 5 (2015) 3540–3551.
[35] X.L. Jin, L.Q. Ye, H. Wang, Y.R. Su, H.Q. Xie, Z.G. Zhong, H. Zhang, Appl. Catal. B: Environ. 165 (2015) 668–675.
[36] J. Wu, H. Lu, X. Zhang, F. Raziq, Y. Qu, L. Jing, Chem. Commun. 52 (2016) 5027–5029.